Li-Salt Doped Single-Ion Conducting Polymer Electrolytes for Lithium Battery Application

(article starts on next page)

Li-Salt Doped Single-Ion Conducting Polymer Electrolytes for Lithium Battery Application

Laura C. Loaiza and Patrik Johansson*

Traditionally solid polymer electrolytes (SPEs) for lithium battery application are made by dissolving a Li-salt in a polymer matrix, which renders both the Li$^+$ cations, the charge carriers of interest, and the anions, only by-standers, mobile. In contrast, single-ion conductors (SICs), with solely the Li$^+$ cation mobile, can be created by grafting the anions onto the polymer backbone. SICs provide the safety, mechanical stability, and flexibility of SPEs, but often suffer in ionic conductivity. Herein an intrinsically synergetic design is suggested and explored; one dopes a promising SIC, LiPSTFSI (poly[(4-styrenesulfonyl)(trifluoromethanesulfonyl)imide]), with a common battery Li-salt, LiTFSI. This way one both increases the Li$^+$ concentration and transport. Indeed, systematically exploring doping, it is found that 50–70 wt% of LiTFSI renders materials with considerable improvements in both the (Li$^+$) dynamics and the ionic conductivity. A deeper analysis allows to address connections between the ion transport mechanism(s) (Arrhenius/VTF), the charge carrier speciation and concentration, and the free volume and glass transition temperature. While no silver bullet is even remotely found, the general findings open paths to be further explored for SPEs in general and Li-salt doped SICs in particular.

1. Introduction

Solid polymer electrolytes (SPEs) at large consist of a polymer acting as a matrix and therein dissolved suitable salts, i.e., Li-salts for lithium batteries.[1] SPEs offer a safer alternative to volatile liquid electrolytes and also some mechanical strength. This is the reason why they were early proposed as solid-state electrolytes (SSEs),[2–4] with renewed interest recently due to the possibility of using lithium metal anodes with SSEs and thereby improve

L. C. Loaiza, P. Johansson
Department of Physics
Chalmers University of Technology
Göteborg SE-41296, Sweden
E-mail: patrik.johansson@chalmers.se
P. Johansson
ALISTORE-European Research Institute
FR CNRS 3104, Hub de l'Energie, 15 Rue Baudelocque, Amiens 80039, France

The ORCID identification number(s) for the author(s) of this article can be found under https://doi.org/10.1002/macp.202100419

lithium battery energy density without compromising safety.[4,5] In practice their utilization as SSEs depends on the flexibility and motion of the polymer chains, which largely determines the ion transport and thereby ionic conductivity, and the Li-salt used, which affects the charge carrier concentration and nature.[6] One archetypical SPE is lithium bis(trifluoromethanesulfonyl)imide, LiTFSI, dissolved in poly(ethylene oxide), PEO, as suggested by Armand.[2] The use of the TFSI anion with its large internal flexibility, bulkiness, and highly delocalized negative charge, both provides a strong plasticizing effect, improving the SPE polymer chain dynamics, and reduces the cation–anion interactions, rendering more charge carriers.[7–11] Such SPEs, however, still suffer from low ionic conductivity at room temperature (RT) and low cation transference numbers, t_+ ≈ 0.2,[12] why they are only functional >70 °C.[13] This is at large the electrolyte design employed in the Bolloré Blue Solutions lithium metal polymer batteries—operating at such elevated temperatures.[14]

Another type of SPEs is single-ion conductors (SICs),[9] wherein the anion is immobilized either by grafting it to the polymer backbone or (less common) by the use of anion capturing receptors.[8,15] Thus, in SICs the cation is the sole conducting species and t_+ is close to unity. This in principle decreases the concentration gradients and the polarization in the cell and should thereby allow for high rate battery cycling.[7,8,16] Unfortunately, most SICs have low ionic conductivities, often even lower than conventional SPEs, e.g., lithium poly[(4-styrenesulfonyl)(trifluoromethanesulfonyl)imide] (LiPSTFSI) at ≈10^{-7}–10^{-8} S cm^{-1} @ RT).[17] This is due to the rigid polymer matrices of SICs and/or the low charge carrier concentrations. To circumvent this strategies of blending, copolymerization, and addition of traditional liquid battery solvents, such as propylene carbonate (PC), have been applied.[8,16,18,19] For example Nederstedt et al.[20,21] prepared an LiPSTFSI–PEO block copolymer SICs and reached ionic conductivities of 10^{-4}–10^{-7} S cm^{-1} at 80 °C; Ma et al.[10] obtained ≈10^{-4} S cm^{-1} at 90 °C for an LiPSTFSI/PEO blend; Feng et al.[17] created an LiPSTFSI-based copolymer reaching 10^{-4} S cm^{-1} at 90 °C; and Bouchet et al.[22] prepared an LiPSTFSI/PEO tri-block copolymer with >10^{-5} S cm^{-1} at 60 °C. Beaudoin et al.[23] also prepared an LiPSTFSI-PEO-LiPSTFSI tri-block copolymer with >10^{-5} S cm^{-1} at 60 °C. Obviously, as compared to liquid electrolytes, these SICs still suffer from (too) low ionic conductivities, even when operated at these elevated temperatures.

**ADVANCED
SCIENCE NEWS**
www.advancedsciencenews.com

[M] macro-
molecular
Chemistry and Physics
www.mcp-journal.de

Here we apply a rather different strategy by increasing the ionic conductivity through doping the SIC with a plasticizer that at the same time provides charge carriers and creates free volume in-between the polymer chains. This follows closely what Matinez-Ibañez et al.[24] pioneered by doping an LiPSTFSI/PEO, thus a blended SIC, with 2 wt% of lithium bis(fluorosulfonyl)imide, LiFSI, reaching up to 10^{-4} S cm^{-1} at 70 °C, and followed by Olmedo-Martínez et al.[25] that reported 2.1×10^{-4} S cm^{-1} at 70 °C for a PEO blend with 50 wt% of PLiMTFSI (poly(lithium 1-[3-(methacryloyloxy) propylsulfonyl]-1-(trifluoromethanesulfonyl) imide).

We, however, here choose to work with "unblended" LiPSTFSI that we dope with the LiTFSI salt in a wide composition range, from 1 to 90 wt%. The aim is to increase the concentration of charge carriers and simultaneously the flexibility of the polymer matrix; but most of all to systematically monitor and correlate the global macroscopic properties, such as the ionic conductivity, glass transition temperature, and mechanical properties, with the local properties, such as speciation and coordination.

2. Results and Discussion

We start by differential scanning calorimetry (DSC) to study the SIC polymer chain dynamics, progress by IR and Raman spectroscopy to address the local interactions, coordination, and charge carriers, and then we employ electrochemical impedance spectroscopy (EIS) to determine the ionic conductivities. From these data, we finally discuss the relationships between them and propose ion transport mechanism(s), e.g., Arrhenius and VTF.

2.1. SIC Polymer Chain Dynamics

Since the ion transport mechanism and the mechanical properties both are intimately dependent on the SIC chain flexibility and dynamics, the glass transition temperature (T_g) is a natural starting point of our study, not the least its changes upon LiTFSI doping. First, however, we note the absence of melting points in the DSC traces, from -100 to +150 °C, indicative of a high degree of amorphicity of both undoped and doped SICs. The T_g of the neat LiPSTFSI SIC is ≈130 °C and upon minor salt addition there are no drastic observable changes until 3 wt%, where the T_g decreases to 50–65 °C (**Figure 1**, **Table 1**). A drastic change appears at 40–50 wt% of LiTFSI where T_gs appear at much lower temperatures, ca. -25 °C and 14 °C, respectively. Subsequent further salt addition produces a continuous decrease in T_g all the way to the maximum 90 wt% of LiTFSI (the trace of pure LiTFSI (100 wt%) is added only for reference).

While the exact behavior of the 50 wt% composition might partly be due to sample thermal history and cannot be fully explained, we here tentatively explain the overall behavior using three regimes i–iii. In *i* the initial few (1–2) wt% of LiTFSI doping disrupts the (short to medium range) ordered structure of the undoped SIC, creating some more local chain dynamics but almost no change in T_g is observed, In regime ii the further salt doping (3–30 wt%) decreases the T_g to 50–65 °C, but some (dynamic) crosslinking must be present to cause the relatively high T_gs obtained. We cannot exclude that the materials are nanophase separated, where the non-cation-coordinated SIC polymer chains are
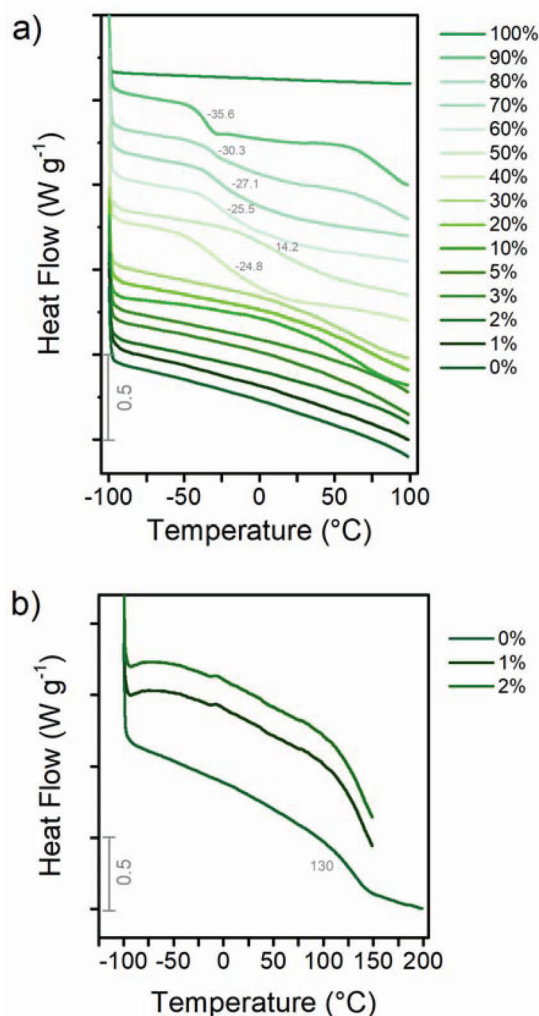

Figure 1. a) Second heating cycle DSC traces as a function of LiTFSI doping, b) extended temperature range cycling for the 0–2 wt% LiTFSI doped systems.

Table 1. Glass transition temperature (T_g) as a function of the LiTFSI doping.

LiTFSI [wt%]	T_g [°C]
0	130
1	130
2	130
3	65.0
5	72.4
10	52.4
20	54.6
30	50.6
40	-24.8
50	14.2
60	-25.5
70	-27.1
80	-30.3
90	-35.6

**ADVANCED
SCIENCE NEWS**

www.advancedsciencenews.com

**Macro-
molecular
Chemistry and Physics**

www.mcp-journal.de

Figure 2. Infrared spectra of LiPSTFSI as a function of LiTFSI doping.

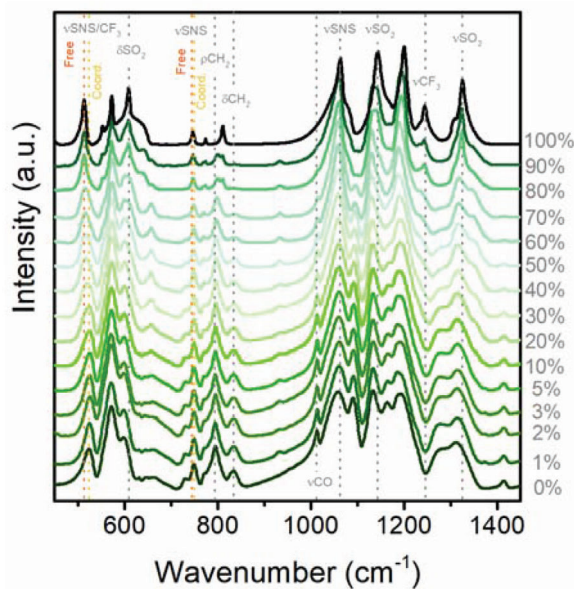**Figure 3.** Raman spectra as a function of LiTFSI doping.

as flexible as those in the less doped compositions. Finally, in iii (40–90 wt%) the excellent plasticizing effect of the TFSI anion[26] is demonstrated as well as the role of free volume being created in-between the polymer chains.[10] Similar behavior has been observed for some ionic rubbers and other plasticized systems.[27] Below we try to prove/disprove the scenario of these regimes i–iii by in detail analyzing the coordination to the SIC polymer chains and the overall speciation in the electrolytes.

2.2. Coordination and Speciation

We analyze the IR and Raman spectra in the fingerprint region to in detail study the ion–polymer chain interactions and the ion–ion interactions, i.e., basically determine the coordination and speciation. Starting with the IR spectra, the bands assigned to the LiPSTFSI SIC (Table S1, Supporting Information[42]) clearly dominate for low LiTFSI doping (**Figure 2**), but it is anyhow possible to identify the evolution of the bands originating in the TFSI anion. Overall, the bands assigned to cation (Li+) coordinated TFSI, at 525 and 746 cm−1, gradually decrease in relative intensity versus the "free" TFSI, at 512 and 740 cm−1. The doublet band at ≈1279 and 1313 cm−1, ascribed to the asymmetric SO2 stretching of the TFSI grafted onto the PS backbone, gradually disappears. Compared to the pure LiTFSI, the band at 1140 cm−1, which is due to symmetric SO2 vibrations, gradually downshifts in frequency, while the doublet due to asymmetric SO2 vibrations gets a bigger separation, and the band from CF3 at 1270 cm−1 more or less vanishes. The cation–anion interactions result in an increase in the electron density that leads to bond weakening and consequently a redshift of the SNS vibrations.[28] Even when looking closely to these details and trying to correlate to the doping regimes i–iii outlined from the DSC data we can, however, only find very rough trends. Indeed, the initial 1–2 wt% LiTFSI doping, regime i above, does not reveal any changes in speciation or coordination. Thereafter, correlating with regime ii, we
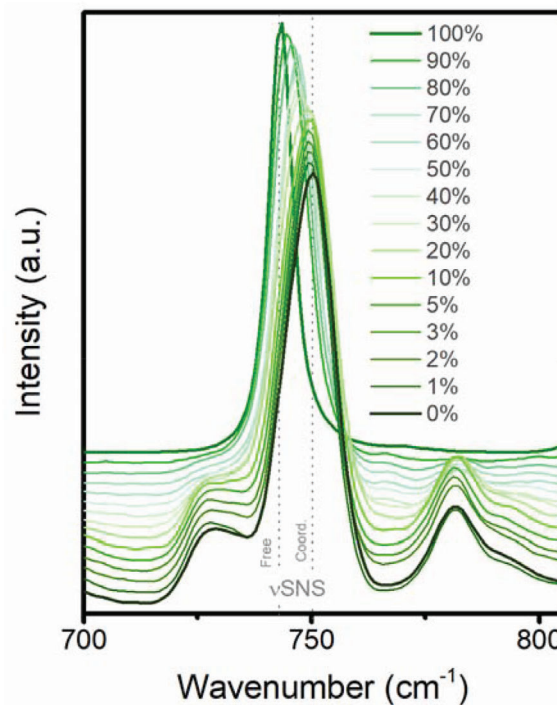
can only indirectly argue for cation-polymer coordination as the added LiTFSI causes "free" TFSI—and thus the added Li+ must coordinate elsewhere, for instance with the polymer backbone "TFSI" part. It is crucial to note that the "TFSI" part of the LiP-STFSI SIC has less contribution in this spectral region as its concentration is somewhat lower: 3.11 M for LiPSTFSI versus 3.48 M for LiTFSI. As for regime iii, the speciation is arguably not decisive for the macroscopic behavior as the plasticizing effect of TFSI does not entail any specific vibrational signal. It is anyhow assuring that the % of "free" TFSI continuously increases all the way up to 90 wt% LiTFSI doping and thus correlates with the decrease in T_g.

Overall similar features can be observed in the Raman spectra as in the IR spectra, where the 250–500 cm−1 region is useful to determine the TFSI anion conformational equilibrium and the in-plane and out-of-plane SO2 vibrations are sensitive to the formation of different Li complexes,[29] thus possible to use to monitor the effects of LiTFSI doping (Figure S2 and Table S2,[42-44] Supporting Information). The focus is, however, as above, on the 700–800 cm−1 region corresponding to the TFSI "all breathing mode,"[29,30] with "free" and Li+-coordinated TFSI assigned at 744 and 750 cm−1, respectively (**Figure 3**). In the deconvolution and band fitting process it is important to acknowledge that the "free" TFSI anion has two conformers that might not be separable and in addition that the "TFSI" from LiPSTFSI will likely have a lower Raman activity. The latter as the corresponding normal mode by necessity is of lower symmetry. For the neat LiPSTFSI SIC, we find two bands at 780 and 728 cm−1, both assigned to the polymer matrix, and a band at 750 cm−1 corresponding to "TFSI" (Figure 3). By stoichiometry, all "TFSI" are always on average cation, i.e., Li+, coordinated. Upon LiTFSI doping all the above bands

**ADVANCED
SCIENCE NEWS**

www.advancedsciencenews.com

**[M] acro-
olecular**

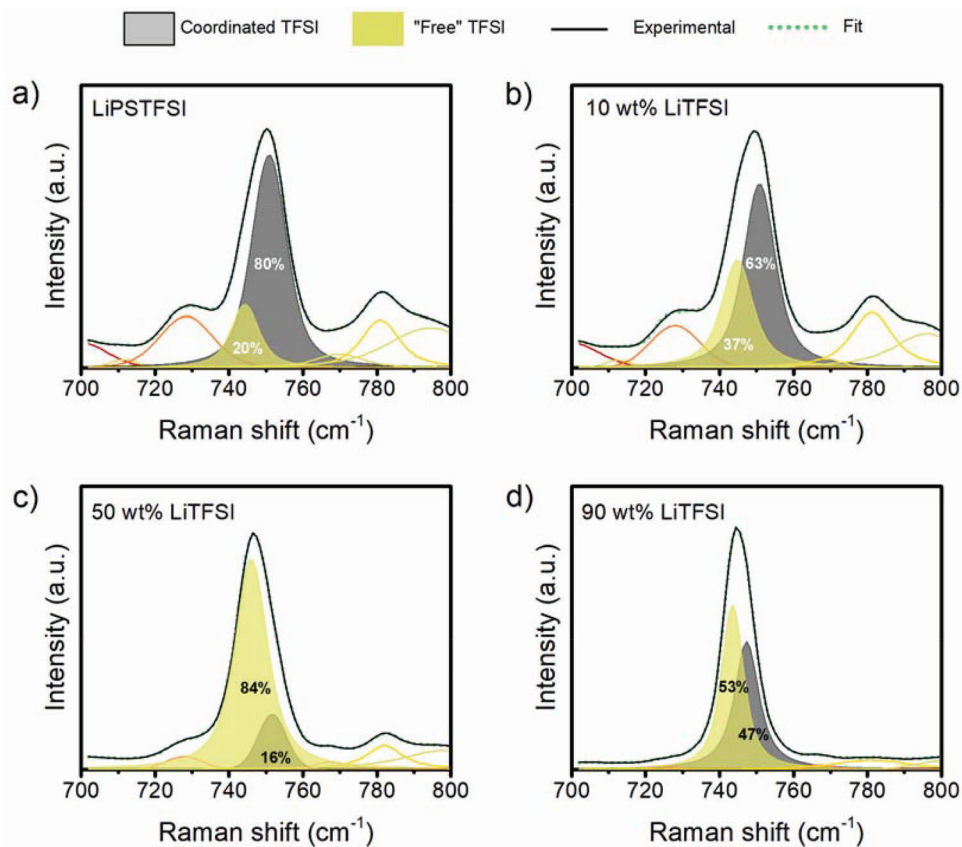**Chemistry and Physics**

www.mcp-journal.de

Figure 4. Deconvoluted Raman spectra for: a) 0, b) 10, c) 50, and d) 90 wt% LiTFSI doping.

evolve and the former two are simply reduced in intensity as the relative LiPSTFSI content decreases. The latter gradually shifts to lower wavenumbers, finally stalling at 744 cm^{-1}, and thus the added LiTFSI salt clearly creates "free" TFSI anions. Even if the exact origin is difficult to determine the permittivity of the system increases, which weakens the ion-ion interactions.

That the "free" TFSI concentration increases as a function of LiTFSI doping also means that some of the Li$^+$ added has to coordinate elsewhere—and the only other possibility available is the formation of (dynamic) ion-polymer interactions/cross-links, which excellently correlates with the macroscopic level observations for regime ii above.

Using the quantitative information available from the deconvolution of Raman spectra, the band areas, show that between 10 and 50 wt% LiTFSI the "free" TFSI contribution increases as function of doping (**Figure 4**). Even for the neat LiPSTFSI, there is a rather significant contribution of "free" "TFSI," ≈20%, a rather surprising result showing that the stoichiometry of 1:1 Li$^+$:"TFSI" allows for different "TFSI" species. The very minor contribution of coordinated TFSI, only 16%, obtained for 50 wt% LiTFSI is striking and in agreement with the discussions above; the Li$^+$ cations thus preferentially coordinate to the SIC polymer chains (or possibly create ionic clusters). The relative increase in coordinated TFSI for 90 wt% points to saturated coordination SIC polymer chain sites and possibly formation of ionic clusters or aggregates. The overall evolution of "free" and coordinated TFSI shows both the very nonlinear behavior and the extremes for 50

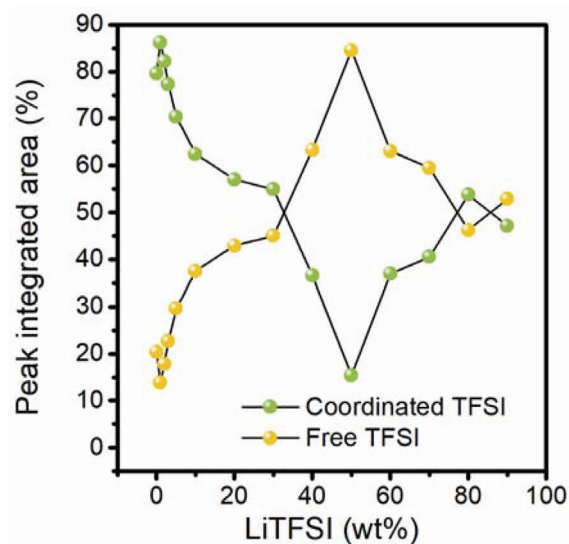**Figure 5.** Evolution of "free" and coordinated TFSI as a function of LiTFSI doping.

wt% LiTFSI doping (**Figure 5**). At ≈50 wt% LiTFSI, we believe that the system changes from salt-in-polymer to polymer-in-salt type and this, including the formation of ionic clusters or aggregates, arguably has impact on the ion transport, e.g., by forma-
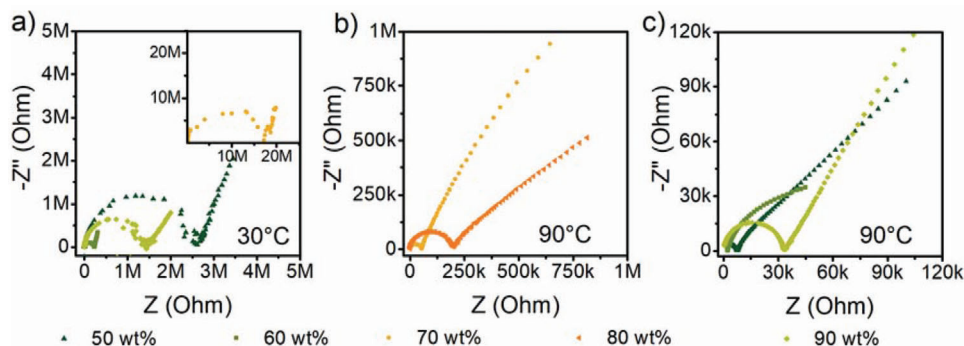
ADVANCED
SCIENCE NEWS
www.advancedsciencenews.com

acro-
molecular
Chemistry and Physics
www.mcp-journal.de

Figure 6. Nyquist plots for 50–90 wt% LiTFSI at: a) 30 °C and b,c) 90 °C.

tion of continuous conduction pathways for Li$^+$ ions.[27] Here, the polymer itself plays a minor role in the ion transport.

2.3. Ionic Conductivity

To address the impact of LiTFSI salt doping and temperature on the ionic conductivity we applied EIS using an asymmetric sample holder in sandwich configuration (Figure S1a, Supporting Information) on a pellet made according to the specifications in Figure S1c (Supporting Information) to obtain the data in **Figure 6**.

The semicircles at high frequencies and straight lines at low frequencies have been fitted with an equivalent circuit (EC), composed of one resistor (R) in parallel with a constant phase element (CPE), i.e., a R//CPE unit, in series with another CPE (Figure S1d, Supporting Information). The first unit accounts for the bulk electrolyte resistance and its non-ideal capacitance, and the second the capacitive effect of the blocking electrodes. CPEs rather than ideal capacitors are used to account for electrode surface roughness. The overall low ionic conductivities (**Figure 7**) put limits to the experimental matrix; at 30 °C only the 50 and 60 wt% LiTFSI doped systems are easily measurable (Figure 6a), the rest (likely) have too large resistances, but at 90 °C there are dramatic decreases in the resistances (Figure 6b,c). This is accompanied by changes in the spectra; the straight line at low frequencies extends over a wider range and the start of the semicircle is no longer visible, in particular for 50 and 60 wt% LiTFSI. In accordance also with the above observations for regimes i,ii, the 1–30 wt% LiTFSI compositions have similar or lower ionic conductivities than the neat LiPSTFSI SIC, due to almost no local structural change and/or the (dynamic) crosslinking induced by the Li-salt addition. For regime iii (40–90 wt% LiTFSI) the ionic conductivity increases, with a maximum at 60 wt% LiTFSI (Figure 7 and **Table 2**).

There is in fact a second semicircle at low frequencies visible in the Nyquist plots for 50–80 wt% LiTFSI and >60 °C, in particular for 60 wt%, but it is absent for 90 wt%. We attribute this to a second ion conduction mechanism and therefore added an additional R2//CPE2 in series to the previous EC. This mechanism is only active at high salt doping and temperatures and contributes less to the total ionic conductivity as compared to the high frequency process (Figure S3, Supporting Information).

An alternative symmetric EIS cell configuration with an interdigitated electrode (Figure S1b, Supporting Information) was
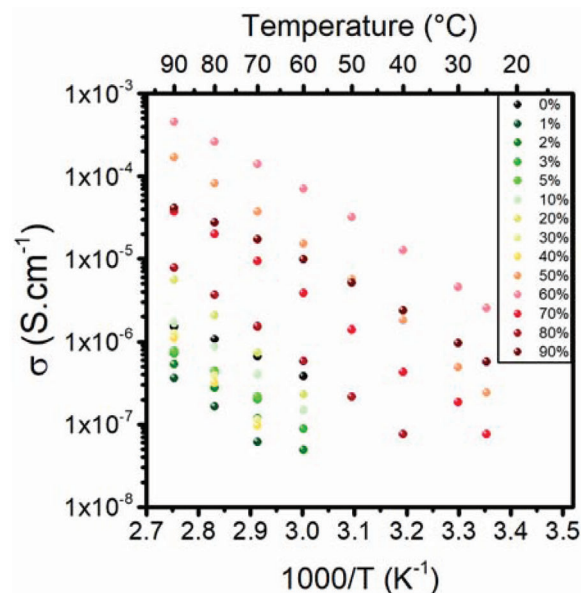

Figure 7. Ionic conductivities obtained using the asymmetric cell as a function of LiTFSI doping: 0, 1, 2, 3, 5, and 10–90%.

Table 2. Ionic conductivity at 90 °C as a function of LiTFSI doping.

LiTFSI [wt%]	σ @ 90 °C [S cm^{-1}]	Standard deviation
0	1.5×10^{-6}	3.2×10^{-7}
1	3.6×10^{-7}	1.2×10^{-7}
2	5.3×10^{-7}	2.9×10^{-7}
3	7.2×10^{-7}	2.2×10^{-7}
5	7.7×10^{-7}	2.8×10^{-7}
10	1.7×10^{-6}	3.5×10^{-7}
20	5.6×10^{-6}	2.2×10^{-6}
30	1.3×10^{-6}	1.3×10^{-7}
40	1.1×10^{-6}	5.7×10^{-7}
50	1.7×10^{-4}	3.1×10^{-5}
60	4.7×10^{-4}	9.9×10^{-5}
70	4.2×10^{-5}	3.1×10^{-5}
80	1.2×10^{-5}	1.3×10^{-6}
90	3.7×10^{-5}	7.1×10^{-6}

**ADVANCED
SCIENCE NEWS**

www.advancedsciencenews.com

{M} acro-
molecular
Chemistry and Physics

www.mcp-journal.de

used to allow for direct casting of the electrolytes onto the electrode and ensure uniformity, e.g., avoid the density variations that easily occur in pellets. In general, the obtained ionic conductivities are somewhat lower as compared to those from the asymmetric cell (Figure S4, Supporting Information), but the trends are similar. Again, >50 wt% LiTFSI doping present the highest ionic conductivities, even if the maximal ionic conductivity as a function of salt doping differs. Differences between symmetric and asymmetric cells have been observed and reported previously and are arguably associated with preferential polymer chain orientations at/in the interdigitated electrode and to the presence of exclusion zones between the different fingers of the electrode which might not be properly taken into account.[31]

2.4. Ion Transport and Conduction Mechanism(s) Analysis

For SPEs and similar electrolytes basically two main modes of ion transport are possible: diffusion (Arrhenius) and matrix relaxation/polymer segmental motion (Vogel-Tammann-Fulcher, VTF).[32] All data suggest our electrolytes to mainly follow an Arrhenius behavior, excepted the 90 wt% LiTFSI doped SIC data (Figure 7) and the 50–90 wt% LiTFSI doped SICs data obtained with the asymmetric EIS cell (Figure S3, Supporting Information). The latter are both better described by a VTF process and can, using arguments for regime iii, be attributed to the TFSI anion plasticizing effect, the increase in free volume, and the formation of ionic clusters/aggregates.

The ionic conductivity data also allow us to make a (semi-)quantitative analysis of the Arrhenius and VTF contributions by a fitting procedure. Above 50 °C, we find the increase in ionic conductivity to become less prominent, which suggests a decrease in the activation energy and that the electrolytes are in a viscous flow state.[10] For low Li-salt doping contents, the dense electrostatic attractions within LiPSTFSI and the (dynamic) crosslinking, renders the matrix very rigid and an Arrhenius behavior.[33] For higher doping contents, there is a delicate balance between increased permittivity which affects redissociation of ion pairs and the formation of triplets and higher aggregates, and the overall decrease in ion mobility.[34] At this stage, the clusters and agglomerates can arguably be arranged in such a way that continuous Li+ conduction pathways are created, percolation threshold is reached, impacting positively the ionic conductivity. This cation transport mechanism might involve activated ion transitions between ionic clusters and cooperative jumps within the matrix.[27,34–36] As we may have an irregular connection between clusters, the polymer chain segmental motions may play a more dominant role in the ion transport mechanism and the ionic conductivity start to decrease.[27,37] The clear Arrhenius to VTF cross-over for the 90 wt% LiTFSI doped composition can be attributed to the above behavior and at the same time the polymer hinders salt precipitation ("salting-out"), both by kinetics and thermodynamics.[27] Overall, the ionic conductivities for, for example, 70 and 90 wt% LiTFSI differ less at higher temperatures than at lower temperatures, a clear sign of the role of the different activation energies (Table S3, Supporting Information).

The changes above also come along with altered mechanical properties; low salt doping contents render brittle electrolytes, much as the neat LiPSTFSI SIC itself has a very rigid polymer
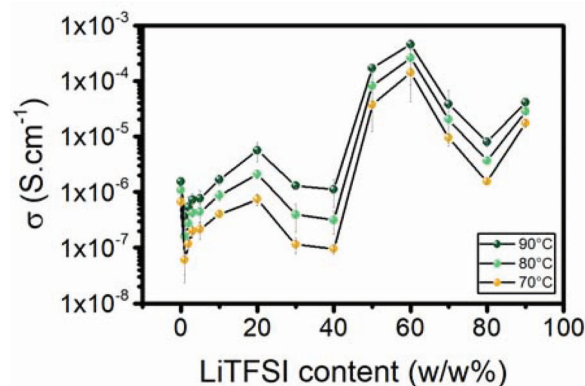

Figure 8. Ionic conductivity for 70–90 °C as a function of LiTFSI doping.

matrix, but further salt doping creates more uniform and gel-like electrolytes—as can also be seen macroscopically (Figure S5, Supporting Information). Note, however, that there is no strict change/borderline between these mechanical properties and the two ion transport and conduction mechanisms as function of doping—given the way that the materials are made, adding Li-salt to a SIC, they are bound to both be present. This also opens for a concerted optimization of mechanical and ion transport properties.

Overall, LiTFSI doping increases the concentration of charge carriers, but when it comes to the flexibility, there are indeed two different scenarios as outlined from the DSC data: until ≈40 wt% LiTFSI the brittleness and (dynamic) crosslinking of the matrix dominate, but beyond ≈50 wt% the plasticizing effect of the TFSI anion becomes more important. This is also reflected in the high-temperature ionic conductivity data— where the added temperature eases the polymer chain dynamics even more and 50–60 wt% creates a maximum (**Figure 8**), which has been observed previously for other concentrated systems.[23,25]

There is no simple rule as to what ion conduction mechanism is to be preferred or the ideal to achieve the higher ionic conductivities, but recent studies have demonstrated the possibility of decoupling the conductivity from the mechanical motions typically at temperatures approaching the T_g, either by creating systems with low T_gs and high contents of aggregated ionic domains,[35,38,39] or as Liu et al.[33] engineer the local environment by placing different anion groups on the side chains of LiPSTFSI. Indeed, for PS-based SICs/SPEs ion transport occur even when the polymer segmental motions are slow.[38]

An important part of analyzing ion transport is to address the cation transference number. The LiPSTFSI as all SICs has a cation transference number close to unity, which has been calculated to in practice be able to "compensate" for an order of magnitude lower ionic conductivity as compared to conventional electrolytes with much lower cation transference numbers.[40] As we add LiTFSI, however, we also add mobile anions. In regime ii, the (added) Li+ cations are suggested to create (dynamic) crosslinks, thus not being very mobile, while most of the TFSI are "free" and thus carry a substantial part of the charge, decreasing the transference number. In regime iii, the relative concentration of "free" TFSI anions is shown to decrease at the expense of formation of ionic clusters and/or aggregates, which could/should point to

**ADVANCED
SCIENCE NEWS**

www.advancedsciencenews.com

**Macro-
molecular
Chemistry and Physics**

www.mcp-journal.de

higher cation transference numbers (again). While we choose to not report any transference numbers herein, some currently preliminary data[46] show promise of high cation transference numbers, up to 0.7, even for the highly salt doped compositions.

3. Concluding Remarks

The strategy to increase the ionic conductivity of LIPSTFSI SICs by doping with LiTFSI and the results obtained from DSC, Raman and IR spectroscopies, and not the least EIS as function of temperature, enable a general discussion of local events affecting global properties. We find that three regimes, i–iii, with unique, albeit not unambiguously identified, modes of ion transport can be argued for and be correlated with Arrhenius and VFT ion transport mechanisms. This comes along with changes in the physical state, as observed by the eye, and arguably also in cation transference numbers. A doping of $\approx$50–60 wt% LiTFSI presents the maximum ionic conductivity, along a maximum in the % of "free" TFSI anions and a change from "salt-in-polymer" to "polymer-in-salt" character,[32] and this is higher than commonly presented for LiPSTFSI copolymers and blends (Table S4,[45] Supporting Information). Yet, the high rigidity of the polymer matrix and a conduction mechanism dependent on ion hopping, renders them less conductive than the best standard SPEs. Doping SICs with LiTFSI or other Li-salts can anyhow be a path to pursue to further improve SPEs with respect to practical application, keeping in mind that there are trade-offs to be made between mechanical properties, the flexibility of the polymer matrix, the concentration of charge carriers, and the speciation.

4. Experimental Section

Materials and Sample Preparation: Poly((trifluoromethane)sulfonimide lithium styrene) (LiPSTFSI, Specific Polymers) was mixed with stoichiometric amounts of lithium bis(trifluoromethanesulfonyl)imide (LiTFSI, Solvionic) (dried at 110 °C overnight) at grams scale, with extra dry acetonitrile (Sigma-Aldrich) as secondary solvent to create the 1, 2, 3, 5, 10–90 wt% LiTFSI doped LiPSTFSI electrolytes/materials. The general sample preparation of each of these mixtures was allowed to stir for 4 h, and subsequently, the secondary solvent was evaporated at room temperature overnight, whereafter the resulting material was vacuum dried at 70 °C for 12 h. Complete solvent removal was confirmed by DSC and Raman spectroscopy. The salt and the polymer are both very soluble in acetonitrile, the secondary solvent used in the preparation stage. There is no sign of neither phase-separation nor salt precipitation in the final products, thus miscibility is inferred, but admittedly this can happen at very long time-scales beyond the scope. All the samples were prepared and stored in an argon-filled glove box (<1 ppm O_2, <1 ppm H_2O). Please note that the exact sample preparation process is slightly different for the symmetric EIS cell configuration (see below).

Differential Scanning Calorimetry (DSC): The DSC measurements were performed using a TA instrument DSC250 under helium atmosphere. The traces were recorded in two heating/cooling cycles, from -100 to 150 °C and a scanning rate of 10 °C min^{-1}. A 20 min isotherm was performed at the maximum and minimum temperatures to remove (parts of) the sample thermal history. TA hermetic aluminum crucibles were loaded with 8–10 mg of sample and sealed inside a glove box. The glass transition temperatures (T_gs) were taken as the midpoint of the heat capacity changes.

Vibrational Spectroscopy: Attenuated total reflectance Fourier-transform infrared spectroscopy (ATR-FTIR) was performed using a Bruker Alpha II compact spectrometer, with a diamond crystal, 2 cm^{-1} resolution, 300 scans, and a range of 400–2000 cm^{-1}. All the measure-

ments were performed inside an argon-filled glove box. Fourier-transform Raman spectroscopy (FT-Raman) was performed using a Bruker Multi-Ram spectrometer equipped with a Nd-YAG 1064 nm laser at an operating power of 400 mW. The spectra were recorded with 2 cm^{-1} resolution, for 6000 scans, and between 200 and 2000 cm^{-1}. The region of the Raman spectrum containing the TFSI "all breathing mode," 700–800 cm^{-1}, was deconvoluted using the PeakFit software and the second derivative method, employing Voigt functions, to account for the Gaussian and Lorentzian contributions from the instrument and different environment effects.

Electrochemical Impedance Spectroscopy (EIS): EIS was performed using a BioLogic VMP3 potentiostat coupled with an intermediate temperature system (ITS) controlling the sample temperature by a Peltier element. All samples were placed in a controlled environment sample holder (CESH) equipped with gold electrodes in either asymmetric (through-plane) or symmetric (in-plane) configuration (Figure S1, Supporting Information). The impedance spectra were recorded for 1–10 mHz, with an excitation voltage of 50 mV, and from 25 °C to 90 °C upon heating and cooling with 10 °C intervals. The CESH was kept at 90 °C for 2 h before the measurement started and the temperature was allowed to stabilize for 1 h at each interval prior to the EIS measurements. For the asymmetric configuration, the samples were pressed in pellets of 6 mm diameter, inside an argon-filled glove box. To ensure an optimal contact between the samples and the gold electrodes, one Papyex (flexible carbon foil, previously dried at 120 °C) and one Cu foil (previously dried at 120 °C) were placed on each side of the pellet, to form a sandwich of Cu/Papyex/sample/Papyex/Cu (Figure S1, Supporting Information). In some cases, a Teflon ring was used to keep the pellet diameter constant. Due to the high resistance for compositions with less than 50 wt% LiTFSI it was only possible to obtain EIS spectra >60 °C.

For the symmetric configuration, the samples were made by direct casting onto the gold electrode. The secondary solvent was allowed to evaporate at room temperature overnight, whereafter the assembly was dried under vacuum for 8 hours. The EIS data was analyzed using Zview software and fitted to different equivalent circuits (ECs) (Figure S1, Supporting Information). Please refer to the main text for the motivation of these ECs. The ionic conductivity was obtained from these fits and data from the asymmetric configuration as (**Equation 1**):

$$\sigma = \frac{D}{R.A} \tag{1}$$

where *D* is the sample thickness, *A* is the sample surface area and R is the resistance. For the symmetric configuration as (Equations 2 and 3):

$$\sigma = \frac{K\text{cell}}{R} \tag{2}$$

and

$$K\text{cell} = \frac{2 * \left(\frac{S}{W}\right)^{1/3}}{L * (N-1)} \tag{3}$$

where *L* and *W* are the finger length and width, respectively, *N* is the number of fingers, and *S* is the finger spacing.[31,41] Finally, the activation energy was calculated from the slope of the plot $\ln(\sigma.T)$ as a function of $1/T$ for the Arrhenius behavior and from $\ln(\sigma.T)$ versus $T_g - T_0$, with $T_0 = T_g - 50$, for the VTF behavior, respectively.

Supporting Information

Supporting Information is available from the Wiley Online Library or from the author.

[1] V. Di Noto, S. Lavina, G. A. Giffin, E. Negro, B. Scrosati, *Electrochim. Acta* **2011**, *57*, 4.
[2] M. B. Armand, *Annu. Rev. Mater. Res.* **1986**, *16*, 245.
[3] P. G. Bruce, C. A. Vincent, *Faraday Discuss. Chem. Soc.* **1989**, *88*, 43.
[4] H. Zhang, M. Armand, *Isr. J. Chem.* **2021**, *61*, 94.
[5] H. Zhang, Y. Chen, C. Li, M. Armand, *SusMat* **2021**, *1*, 24.
[6] C. Austen Angell, *Electrochim. Acta* **2019**, *313*, 205.
[7] H. Zhang, F. Chen, O. Lakuntza, U. Oteo, L. Qiao, M. Martinez-Ibañez, H. Zhu, J. Carrasco, M. Forsyth, M. Armand, *Angew. Chem., Int. Ed.* **2019**, *58*, 12070.
[8] H. Zhang, C. Li, M. Piszcz, E. Coya, T. Rojo, L. M. Rodriguez-Martinez, M. Armand, Z. Zhou, *Chem. Soc. Rev.* **2017**, *46*, 797.
[9] H. Zhang, Z. Song, W. Yuan, W. Feng, J. Nie, M. Armand, X. Huang, Z. Zhou, *ChemElectroChem* **2021**, *8*, 1322.
[10] Q. Ma, Y.u Xia, W. Feng, J. Nie, Y.-S. Hu, H. Li, X. Huang, L. Chen, M. Armand, Z. Zhou, *RSC Adv.* **2016**, *6*, 32454.
[11] J. Olmedo-Martínez, L. Meabe, A. Basterretxea, D. Mecerreyes, A. Müller, *Polymers* **2019**, *11*, 452.
[12] P. Deng, H. Zhang, W. Feng, Z. Zhou, M. Armand, J. Nie, *Solid State Ionics* **2019**, *338*, 161.
[13] M. A. Ratner, D. F. Shriver, *Chem. Rev.* **1988**, *88*, 109.
[14] "Bolloré," https://www.bollore.com/en (accessed: Dec 10, 2021), **n.d**.
[15] K. Xu, *Chem. Rev.* **2014**, *114*, 11503.
[16] K. Jeong, S. Park, S.-Y. Lee, *J. Mater. Chem. A* **2019**, *7*, 1917.
[17] S. Feng, D. Shi, F. Liu, L. Zheng, J. Nie, W. Feng, X. Huang, M. Armand, Z. Zhou, *Electrochim. Acta* **2013**, *93*, 254.
[18] A. Manuel Stephan, *Eur. Polym. J.* **2006**, *42*, 21.
[19] J. Lopez, D. G. Mackanic, Y.i Cui, Z. Bao, *Nat. Rev. Mater.* **2019**, *4*, 312.
[20] H. Nederstedt, P. Jannasch, *ACS Appl. Energy Mater.* **2020**, *3*, 9066.
[21] H. Nederstedt, P. Jannasch, *Polym. Chem.* **2020**, *11*, 2418.
[22] R. Bouchet, S. Maria, R. Meziane, A. Aboulaich, L. Lienafa, J.-P. Bonnet, T. N. T. Phan, D. Bertin, D. Gigmes, D. Devaux, R. Denoyel, M. Armand, *Nat. Mater.* **2013**, *12*, 452.
[23] E. Beaudoin, T. N. T. Phan, D. Gigmes, E. Giroud, P. Davidson, R. Bouchet, *Electrochim. Acta* **2018**, *269*, 250.
[24] M. Martinez-Ibañez, E. Sanchez-Diez, L. Qiao, Y. Zhang, X. Judez, A. Santiago, I. Aldalur, J. Carrasco, H. Zhu, M. Forsyth, M. Armand, H. Zhang, *Adv. Funct. Mater.* **2020**, *30*, 2000455.
[25] J. L. Olmedo-Martínez, L. Porcarelli, Á. Alegría, D. Mecerreyes, A. J. Müller, *Macromolecules* **2020**, *53*, 4442.
[26] S. Sylla, J.-Y. Sanchez, M. Armand, *Electrochim. Acta* **1992**, *37*, 1699.
[27] M. Forsyth, J. Sun, D. R. Macfarlane, A. J. Hill, *J. Polym. Sci., Part B: Polym. Phys.* **2000**, *38*, 341.
[28] N. R. Dhumal, S. P. Gejji, *J. Mol. Struct.: THEOCHEM* **2006**, *758*, 233.
[29] M. Herstedt, M. Smirnov, P. Johansson, M. Chami, J. Grondin, L. Servant, J. C. Lassègues, *J. Raman Spectrosc.* **2005**, *36*, 762.
[30] D. Brouillette, D. E. Irish, N. J. Taylor, G. Perron, M. Odziemkowski, J. E. Desnoyers, *Phys. Chem. Chem. Phys.* **2002**, *4*, 6063.
[31] A. Maurel, M. Armand, S. Grugeon, B. Fleutot, C. Davoisne, H. Tortajada, M. Courty, S. Panier, L. Dupont, *J. Electrochem. Soc.* **2020**, *167*, 070536.
[32] J. Mindemark, M. J. Lacey, T. Bowden, D. Brandell, *Prog. Polym. Sci.* **2018**, *81*, 114.
[33] J. Liu, P. D. Pickett, B. Park, S. P. Upadhyay, S. V. Orski, J. L. Schaefer, *Polym. Chem.* **2020**, *11*, 461.
[34] S. Lascaud, M. Perrier, A. Vallee, S. Besner, J. Prud'homme, M. Armand, *Macromolecules* **1994**, *27*, 7469.
[35] A. Kisliuk, V. Bocharova, I. Popov, C. Gainaru, A. P. Sokolov, *Electrochim. Acta* **2019**, *299*, 191.
[36] S. Arumugam, J. Shi, D. P. Tunstall, C. A. Vincent, *J. Phys.: Condens. Matter* **1993**, *5*, 153.
[37] J. T. Bendler, J. J. Fontanella, M. F. Shlesinger, M. C. Wintersgill, *Electrochim. Acta* **2003**, *48*, 2267.
[38] Y. Wang, A. L. Agapov, F. Fan, K. Hong, X. Yu, J. Mays, A. P. Sokolov, *Phys. Rev. Lett.* **2012**, *108*, 088303.
[39] Y. Fu, V. Bocharova, M. Ma, A. P. Sokolov, B. G. Sumpter, R. Kumar, *Phys. Chem. Chem. Phys.* **2017**, *19*, 27442.
[40] M. Doyle, T. F. Fuller, J. Newman, *Electrochim. Acta* **1994**, *39*, 2073.
[41] M. Ibrahim, J. Claudel, D. Kourtiche, M. Nadi, *J. Electr. Bioimpedance* **2013**, *4*, 13.
[42] J.-C. Lassègues, J. Grondin, C. Aupetit, P. Johansson, *J. Phys. Chem. A* **2009**, *113*, 305.
[43] L. Suo, F. Zheng, Y.-S. Hu, L. Chen, *Chin. Phys. B* **2015**, *25*, 016101.
[44] J. Pitawala, A. Martinelli, P. Johansson, P. Jacobsson, A. Matic, *J. Non.-Cryst. Solids* **2015**, *407*, 318.
[45] Q. Ma, H. Zhang, C. Zhou, L. Zheng, P. Cheng, J. Nie, W. Feng, Y. S. Hu, H. Li, X. Huang, L. Chen, M. Armand, Z. Zhou, *Angew. Chem. , Int. Ed.* **2016**, *55*, 2521.
[46] L. C. Loaiza, D. Bernin, P. Johansson, preliminary data - to be published **2022**.